J. Fluid Mech. (1999), *vol.* 382, *pp.* 307–329. Printed in the United Kingdom

Large- and small-scale vortical motions in a shear layer perturbed by tabs

By JUDITH K. FOSS† AND K. B. M. Q. ZAMAN

NASA Lewis Research Center, Cleveland, OH 44135, USA

(Received 17 December 1997 and in revised form 8 October 1998)

The large- and small-scale vortical motions produced by 'delta tabs' in a two-stream shear layer have been studied experimentally. An increase in mixing was observed when the base of the triangular shaped tab was affixed to the trailing edge of the splitter plate and the apex was pitched at some angle with respect to the flow axis. Such an arrangement produced a pair of counter-rotating streamwise vortices. Hot-wire measurements detailed the velocity, time-averaged vorticity (Ω_x) and small-scale turbulence features in the three-dimensional space downstream of the tabs. The small-scale structures, whose scale corresponds to that of the peak in the dissipation spectrum, were identified and counted using the peak-valley-counting technique. The optimal pitch angle, θ, for a single tab and the optimal spanwise spacing, S, for a multiple tab array were identified. Since the goal was to increase mixing, the optimal tab configuration was determined from two properties of the flow field: (i) the large-scale motions with the maximum Ω_x, and (ii) the largest number of small-scale motions in a given time period. The peak streamwise vorticity magnitude $|\Omega_{x\_max}|$ was found to have a unique relationship with the tab pitch angle. Furthermore, for all cases examined, the overall small-scale population was found to correlate directly with $|\Omega_{x\_max}|$. Both quantities peaked at $\theta \approx \pm 45°$. It is interesting to note that the peak magnitude of the corresponding circulation in the cross-sectional plane occurred for $\theta \approx \pm 90°$. For an array of tabs, the two quantities also depended on the tab spacing. An array of contiguous tabs acted as a solid deflector producing the weakest streamwise vortices and the least small-scale population. For the measurement range covered, the optimal spacing was found to be $S \approx 1.5$ tab widths.

1. Introduction

Mixing enhancement has many technological benefits and is, therefore, an area of continuing research. Various control schemes have been examined in an effort to increase mixing in different flows. A common strategy in these schemes has been to manipulate the large-scale vortical motions indigenous to the shear region. Primarily, these are the spanwise vortical structures that characterize all two-dimensional shear layers. Another form of the large-scale structures, receiving renewed attention lately, are the steady streamwise vortices, e.g. those produced by vortex generators. The large structures, in any of these forms, play a crucial role in the dynamics of the shear layer. They are responsible for the bulk of the entrainment and transfer of mass and momentum across the shear region. Thus, an understanding of their dynamics and interaction is critical for the implementation of any mixing enhancement scheme.

---

† Now with Dynacs Engineering Co., Inc. (Icing Research Branch, NASA Lewis).

Enhancing the large-scale mixing, however, is only the first step. The ability to mix at the small scales is equally critical. In jet engine applications, for example, a more efficient small-scale mixing is expected to reduce noise via the elimination of 'hot spots' as well as by shifting the energy to higher frequency bands. For reacting flows, mixing at the small-scales is essential so that the molecules combine effectively. Thus, obtaining a clear understanding of the dynamics of the small-scale structure, *vis-à-vis* the large-scale structure dynamics, is also important.

In the present experimental study, large structures in the form of streamwise vortex pairs are introduced in a two-stream layer using delta tabs. In several previous experiments, tabs have proved to be effective in increasing overall mixing. For example, in a comparative survey of jet mixing with various nozzle shapes, Zaman (1996) found geometry involving delta tabs far exceeded the performance of other nozzle shapes. The survey included a 'lobed' geometry as well as rectangular and elliptic nozzles for both subsonic and supersonic flow regimes.

The present investigation is to advance the understanding of the effect of tabs on the flow field. The objectives are stated in § 1.3. First, past studies on the effect of tabs are reviewed in § 1.1, followed by a brief account of pertinent studies on small-scale turbulent structures in § 1.2.

1.1. *Effect of tabs on jets*

Bradbury & Khadem (1975) were among the first to document the effect of tabs in a low-speed jet. With square tabs placed normal to the flow at the nozzle exit, they observed an accelerated centreline velocity decay and a profound distortion of the velocity field in the cross-stream plane. They speculated that the azimuthal vorticity had been significantly disrupted, and that this had the potential for noise reduction. Ahuja & Brown (1989) saw this dramatic reduction in centreline velocity for supersonic conditions as well. They verified the elimination of the screech tone for underexpanded supersonic jets caused by the tabs (Tanna 1977), and speculated that 'though the axisymmetric structures are suppressed, other large-scale motions are present' which must be responsible for the phenomenal entrainment. Subsequent researchers (e.g. Zaman, Reeder & Samimy 1994; Bohl & Foss 1996) have clearly determined that the tab produces a pair of counter-rotating streamwise vortices. The sense of rotation of the vortex pair is such that fluid from the centre of the tab base flows towards its tip. The relative magnitude of the peak streamwise vorticity was found to be about 20% of that of the peak azimuthal vorticity for a tabbed circular jet at a Mach number of 0.3 (Zaman 1993).

Zaman (1993) and Zaman *et al.* (1994) surmised two possible sources of streamwise vorticity for the flow over a tab (J. F. Foss first suggested these two sources, see also Bohl & Foss 1996). The dominant source (source 1) comes from the 'pressure hill' formed upstream of the tab. The flow deceleration by the tab creates a pressure hill, which together with the presence of the wall, produces the pair of counter-rotating streamwise vortices. This mechanism is described mathematically by the Navier–Stokes equation applied at the wall,

$$\left.\frac{1}{\rho}\frac{\partial p}{\partial z}\right|_{y=0} = \nu \left.\frac{\partial}{\partial y}(\omega_x)\right|_{y=0},$$

where y and z are the lateral (normal to the wall) and spanwise coordinates, respectively, and the substitution, $\omega_x|_{y=0} = \partial w/\partial y$, has been made. The secondary source (source 2), again owing to the pressure gradients on the tab's surface, is the vorticity shed from the sides of the tab. Initially, vorticity is shed parallel to the edge; as it convects downstream, it becomes reoriented by the velocity gradients in the shear layer. Thus, if the tab is tilted downstream, vorticity from sources 1 and 2 add together, improving the tab's effectiveness (Zaman *et al.* 1994). In addition to the pressure gradients which flux streamwise vorticity into the flow, the well-known 'necklace' or 'horseshoe' vortices due to boundary-layer reorientation can also be important in the flow over a tab. Several researchers (Bohl & Foss 1996; Reeder & Samimy 1996) have detected the cores of the necklace vortices. It should be noted that the sense of rotation of the vortex pair from the pressure hill is always opposite to that of the necklace vortex pair.

Several other observations regarding optimal tab placement and shape have been made. Reeder & Zaman (1996) found that the tab is best placed at the trailing edge. Upstream or detached settings interfere with the pressure hill source of vorticity. Also, the tab height must exceed the boundary-layer thickness to generate streamwise vorticity effectively. However, tabs with a much smaller height can produce noticeable effects. In a chemically reacting, compressible, two-stream shear layer, Island, Urban & Mungal (1998) observed a significant increase in product formation and thickening of the shear layer when a tab with a height of only 5% of the boundary-layer displacement thickness was placed at the trailing edge. After brief parametric studies, both Zaman *et al.* (1994) and Island *et al.* (1998) found the optimal tab shape to be triangular. In the usage of Zaman *et al.*, the base of the tab was attached to the exit edge of a nozzle and the apex tilted downstream at 45°. This configuration not only worked as effectively as a square tab placed normal to the flow but also incurred less thrust penalty.

While most of the investigations on the effect of tabs have been conducted experimentally, there have also been a few numerical studies (e.g. Grosch *et al.* 1997; Steffen, Reddy & Zaman 1997). Steffen *et al.* compared numerical results with corresponding experimental results and noted good agreement in terms of the vorticity field as well as overall jet entrainment. These results lent further credence to the postulations made on the basic flow dynamics as discussed above.

Most of the studies cited in the foregoing were conducted in free jets discharging into quiescent surroundings. Ahuja (1993) and Carletti, Rogers & Parekh (1995) investigated the effect of the tabs for a circular jet with a cylindrical ejector surrounding the jet. Both found an increased mixing within the ejector under the influence of the tabs. However, a systematic fundamental study for the effect of tabs in the presence of a co-flow has been lacking. Similarly, while most of the investigations addressed overall mixing, only a few attempted to study the small-scale mixing. These are discussed in the next section. The deficiencies in the understanding of the effect of tabs are discussed further in § 1.3.

1.2. *Small-scale structures*

General studies of streamwise vorticity interacting with spanwise vorticity (shear layers) have repeatedly demonstrated locally elevated turbulence. For example, Huang & Ho (1990), Bell & Metha (1990, 1993), Nygaard & Glezer (1991) and Gretta & Smith (1993) found increased normal stresses, $\overline{u_i^2}$ and Reynolds stresses $\overline{u_i u_j}$, in the core of the spanwise vortical structures and in the vicinity of the streamwise vortical structures. Cetegen & Aguirre (1990) performed an analysis on a counter-rotating pair of vortices in a flow with fast reaction chemistry. They found a direct relationship between the molecular mixing and the vortex strength. That is, the stronger the vortex, the greater the molecular mixing. Flow visualizations and concentration measurements in water jets from both Zhang & Schneider (1995) and Hu *et al.* (1996) indicated that small-scale structures appeared earlier with a tab; i.e. the ‘mixing transition’ moved upstream. Zhang & Schneider also showed that an increase in the overall jet spreading caused by a tab was accompanied by an increase in product formation.

Huang & Ho (1990) introduced the peak-valley-counting (PVC) technique to directly detect the small-scale structures believed to be responsible for the mixing transition. This technique is described in § 2. They examined the concentration of small-scale structures relative to the spanwise and streamwise large-scale structures in a two-stream, initially laminar, shear layer. Small-scale transition occurred a short distance downstream of the first spanwise vortex pairing location, and the small-scale structures were concentrated in the centre of the time-averaged shear layer. However, instead of being uniformly distributed in the span, concentrations were greatest near the cores of the streamwise vorticity. They speculated that ‘the small-scale transition is produced by the strain field of the merging (spanwise) vortices imposed on the streamwise vortices, the strained streamwise vortices were unstable and originated the random fine scale turbulence.’

Zohar & Ho (1996) demonstrated that the frequency of the small-scale eddies detected by the PVC code matched the peak in the three-dimensional dissipation spectrum. As an additional check, Foss (1994) found a nominally one-to-one correlation between the small-scale population distribution and the distributions of the dissipation terms, $\overline{(\partial u_i/\partial x_j)^2}$. This clearly indicated that the small-scale structures under consideration were primarily responsible for the dissipation of turbulent kinetic energy. Zohar & Ho furthermore observed that increasing the two-dimensional acoustic forcing level applied to the shear layer increased the small-scale populations around the second spanwise vortex pairing location. Specifically, using phase-averaged data over one spanwise vortex passage, they found that the small-scale eddies were concentrated overwhelmingly (10:1) in the core of the spanwise vorticity, or ‘roller’ region and not in the ‘braid’ region, between rollers. The water channel experiments of Nygaard & Glezer (1991) as well as the direct numerical simulations of Moser & Rogers (1993) also suggested a similar distribution. These two studies showed that the small-scale structures appeared first with the merging of the spanwise vorticity and near the three-dimensional streamwise vortical structures (‘ribs’).

1.3. *Objectives*

As stated above, the purpose of the present experiment was to advance the understanding of the effect of tabs on the flow field within mixing layers. It was motivated by a lack of clear understanding in several areas: (i) the effect of tabs on the small-scale turbulent structures, (ii) the effect of the tab in the presence of a co-flow, and (iii) the impact of the geometry of an array of tabs on the flow field. It was felt that an experiment in the simplest of flows, namely, a two-stream planar mixing layer, would be appropriate to address these effects. This led to the present experiment that was designed to study the effect of parametric variation of a single tab and the geometry of an array of tabs on the flow downstream. Detailed measurements of the streamwise vortical structures and the concomitant small-scale structures were planned. Because previous studies indicated that the dynamics of the tab-generated streamwise vortices were essentially the same at different Mach numbers (Zaman *et al.* 1994), this research was afforded several luxuries. Specifically, the speed was decreased to increase the Kolmogorov scale, and the physical size of the tab was increased to allow higher probe resolution. The effect of pitch angle of a single tab was studied first. The downstream evolution of the flow field for an optimum angle case was addressed next. Finally, in anticipation that most applications would involve an array of tabs, the optimal

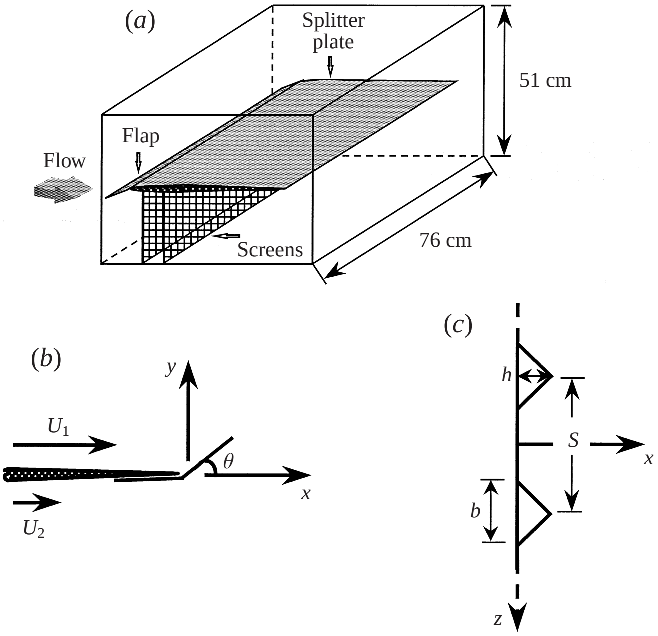

FIGURE 1. Schematic of (*a*) test section and splitter plate, tabs and coordinate system, (*b*) side view, (*c*) plan view.

spacing between tabs was examined. The optimal condition was determined by both a maximum small-scale population and a maximum magnitude of the time-averaged streamwise vorticity.

2. Experimental facility and procedure

The flow field for the study was a two-stream plane mixing layer generated in a 51 cm × 76 cm low-speed wind tunnel. The open loop, induction-type (i.e. fan on the downstream end) tunnel had less than 0.1% turbulence intensity in the test section. To generate the mixing layer for this experiment, a 33 cm chord symmetric splitter plate was installed that spanned the test section at midheight. The essential features of the test section are shown schematically in figure 1 (*a*). The maximum thickness of the plate was 1.27 cm and it tapered down to 0.05 cm at the trailing edge. This plate sat on a frame (not shown in figure 1 (*a*) for clarity) that also housed two screens. The resulting flow had uniform streams above and below the plate with a nominal velocity ratio of 2:1. Through initial diagnostic experiments, a flap was placed at the leading edge and tilted into the low-speed side to avoid laminar separation near the leading edge of the upper (high-speed) surface.

The high-speed velocity was fixed at $U_1 = 9.32\,\mathrm{m\,s^{-1}}$, and the low-speed velocity at $U_2 = 4.55\,\mathrm{m\,s^{-1}}$. The shear velocity, $\Delta U = U_1 - U_2$, was used for data normalization. The boundary-layer thicknesses at the trailing edge were 1.22 cm and 0.71 cm for the high- and low-speed sides, respectively. The corresponding shape factors were 1.5 and 2.0, and the momentum thickness Reynolds numbers were $Re_\theta = 932$ and 193, respectively. The boundary layers at the plate trailing edge were nominally turbulent on the upper surface and nominally laminar on the lower surface; the difference in state explains a thicker boundary layer on the high-speed side. No identifiable peak existed in the velocity spectra on either side.

The delta tab was a triangular piece of 0.025 cm thick metal shim with a base width, $b = 2.54\,\text{cm}$, and a height, $h = 1.27\,\text{cm}$. The angle at the apex was 90°. The base was fixed to the splitter plate trailing edge and the apex was tilted into the flow. The characteristic lengthscale for data normalization was the tab width, b. This choice was based on the finding that the flow field was more sensitive to the width of the tab than to its height (Zaman *et al.* 1994).

The coordinate system, shown in figure 1(*b*) and 1(*c*), had its origin at the trailing edge of the splitter plate and at the symmetry plane. For the single tab case, this was coincident with the tab centre. The side view in figure 1(*b*) illustrates how the tab pitch angle, θ, was defined relative to the free-stream direction. For the multiple tab case, the coordinate origin was located at the midpoint between the central two tabs. The plan view of figure 1 (*c*) illustrates only the central two tabs of the multiple tab case. During the multiple tab experiments, four tabs were spaced at a distance $S = S^*/b$ apart as measured between tab centres. The superscript (*) is used to indicate dimensional quantities.

The measurements were conducted using standard hot-wire anemometry. The velocity and small-scale data were taken with a single straight wire; the streamwise vorticity measurements were conducted with two X-wire arrays. Both the single hot-wire (TSI 1260A-T1.5) and the two X-wires (TSI 1241-T1.5) were made of tungsten with diameters of 4 μm. The single wire had a length of 1.25 mm with a flat frequency response up to 30 kHz. The total sample time was 12.3 s. Stationarity of all parameters considered was achieved after approximately 9 s.

Two X-wire arrays were used to acquire the data for the mean streamwise vorticity which was estimated as $\Omega_x = (\Delta W/\Delta Y - \Delta V/\Delta Z)$. One array was placed in the 'u, v', and the other in the 'u, w', orientation. The probes were spaced 2.64 cm apart in the span and were traversed so that they sampled at the same points in space, but at different times. The v and w data were corrected for the error introduced by the mean shear and the finite separation of the sensors in each X-array according to standard procedures (Bell & Metha 1993). The sampling rate for these data was 500 Hz. Further description of the two-X-wire technique can be found in Zaman (1993). It should be noted that vorticity amplitude approximated by this technique agreed well with corresponding data obtained by two passes (one per orientation) of a single X-wire. The single X-wire was yaw tested in the 'u, w'-orientation. At 20° yaw, the measured streamwise velocity overestimated the actual by 1.8%. The secondary velocity (w) recorded a 4.4% increase. All data, therefore, were sampled downstream of $X = 1.0$, where the average flow angles were less than 20°.

Data were taken in cross-stream (Y, Z) planes at several downstream locations. Facility limitations prevented measurements downstream of $X = 8.5$. Data taken in the transverse direction, Y, extended into the potential flow regions on either side of the shear layer. For the single-wire measurements of velocity and small-scale population, the step size was $\Delta Y = 0.1$ in the shear region, and $\Delta Z = 0.125$ to 0.250 behind the tab. For the streamwise vorticity measurements, the effect of grid density was checked according to the method outlined by Zaman (1993). This involved measurement of Ω_x, in the region of peak streamwise vorticity, by line integration of the velocities around a single grid. The grid size was decreased until the amplitude of Ω_x became independent of the grid size. Based on these preliminary studies, the data were taken with the spacings, $\Delta Y = \Delta Z = 0.13$.

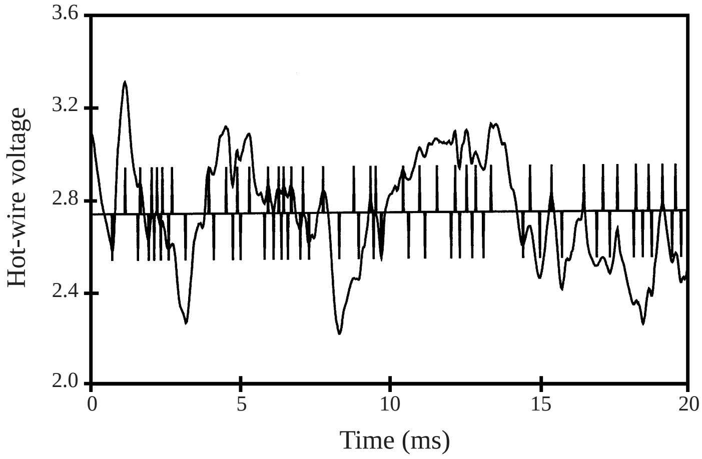

FIGURE 2. Peak-valley-counting technique depicting the velocity trace and pulse train.

2.1. *Peak-valley-counting technique*

The peak-valley-counting (PVC) technique was designed to detect the fine-scale eddies directly from a velocity trace. In the same manner that a passing large-scale coherent structure leaves its signature on a velocity trace, a small-scale eddy – provided the sensor resolutions are sufficient to measure it – can also leave a detectable signature in the velocity time series. That is, the local extrema in the trace are the signatures of the small-scale eddies. The PVC code constructs a pulse train to identify these local peaks and valleys. Such a velocity trace and pulse train is shown in figure 2. See Zohar & Ho (1996) for further details.

Several diagnostics may be performed once the pulse train has been established. The small-scale population, N^*, is proportional to the sum of all the pulses. The time between adjacent pulses is half the period of a fine-scale structure. A histogram of these frequencies, or inverse periods, yields a fairly sharp distribution centred around a 'most probable frequency'. As will be shown (in figure 11), this peak frequency matches the peak frequency of the pseudodissipation spectrum. For this paper, the pseudodissipation spectrum is estimated from the measurable one-dimensional energy spectrum, figure 11, and is defined as $D(\kappa_1) = 2\nu \int \kappa_1^2 F_{11}(\kappa_1) \mathrm{d}\kappa_1$, where $\kappa_1 = 2\pi f/\overline{U}$, f is the frequency, and $\overline{U}$ is the mean velocity. The PVC thresholds for the five filtering sequences necessary to distinguish between flow structure and noise were, in fact, set by comparison with $D(\kappa_1)$. That is, hot-wire data recorded at various x and y near the centre of the shear layer were processed through both the pseudodissipation calculation and the PVC code. Once the thresholds were set, this procedure was repeated at a higher velocity to check the robustness of the thresholds. Indeed, the peaks of both curves shifted to the same higher frequency.

As stated earlier, application of the code requires sufficient frequency response and spatial resolution of the sensor, as well as a sufficiently fast sampling rate to describe the scale of interest. The PVC data were acquired with the straight wire at a sampling rate of 20 kHz, fast enough to resolve the fine scales. An evaluation of the data showed that the maximum frequency of the small-scale structures was 4 kHz, which was well within the 30 kHz response of the wire. The dissipative eddy length – as determined by Taylor's hypothesis – to sensor length ratio was 1.38. Initial tests

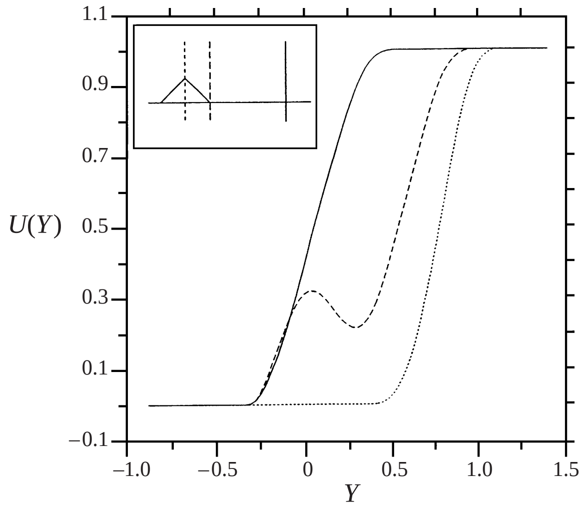

FIGURE 3. Mean velocity profiles, $U(Y\,;Z)$, for a single tab at $X = 4.0$ and $\theta = 45°$; —, $Z = 2.0$; - - -, 0.5; $\cdots$, 0.

determined that the small-scale results remained unchanged for a faster digitizing rate of 50 kHz.

3. Results

3.1. *Single tab*; *angle variation*

Experiments were conducted with a single tab pitched into both the high ($\theta > 0°$) and low ($\theta < 0°$) speed sides. The specific values were: $\theta = 0°$, $\pm 15°$, $\pm 30°$, $\pm 45°$, $\pm 60°$, $\pm 90°$, $\pm 135°$. The data were sampled at a fixed downstream location, $X = 4.0$, where the large-scale vortical motions had had a chance to mature but not diffuse.

For orientation purposes, mean streamwise velocity profiles at three spanwise locations, $U(Y\,;Z)$, are presented in figure 3. The velocity, $U = (U^* - U_2)/(U_1 - U_2)$, was normalized so that its values varied from zero (0) in the low-speed free stream to unity (1) in the high-speed free stream. The three profiles depicted in figure 3 were taken for $\theta = 45°$ at $Z = 0.0$, 0.5 and 2.0. The profile at $Z = 2.0$ is similar to that of the traditional two-dimensional mixing layer hyperbolic tangent profile. The profile at the apex, $Z = 0.0$, is also similar, but is shifted in Y and is nominally 30% thinner in both momentum and vorticity thicknesses. The profile at the base edge of the tab, $Z = 0.5$, on the other hand, is dramatically different. Here, the time-averaged mean velocity profile has a 'bump' in it; that is, a second, inviscidly unstable inflection point has been added. As will be demonstrated later, peaks in both streamwise vorticity and small-scale populations occur in the vicinity of this distortion.

A more comprehensive picture of the effect of the tab can be obtained from the data on a cross-stream (Y, Z) plane. Figure 4 shows mean velocity contour plots at various pitch angles, $U(Y, Z\,;\theta)$. The splitter plate trailing edge and the tab are depicted with a dashed line for reference. The middle two contours bound the locus of the half velocity points, that is, the centre of the time-averaged spanwise vorticity, Ω_z. The data for $\theta = 45°$ are shown in figure 4(*d*). The mean velocity profile bump, seen in figure 3, is now manifest by a 'horseshoe'-shaped contour. This occurs for $\theta = 60°$ (figure 4*c*) and 45° (as well as for 30°, the data for which are not included

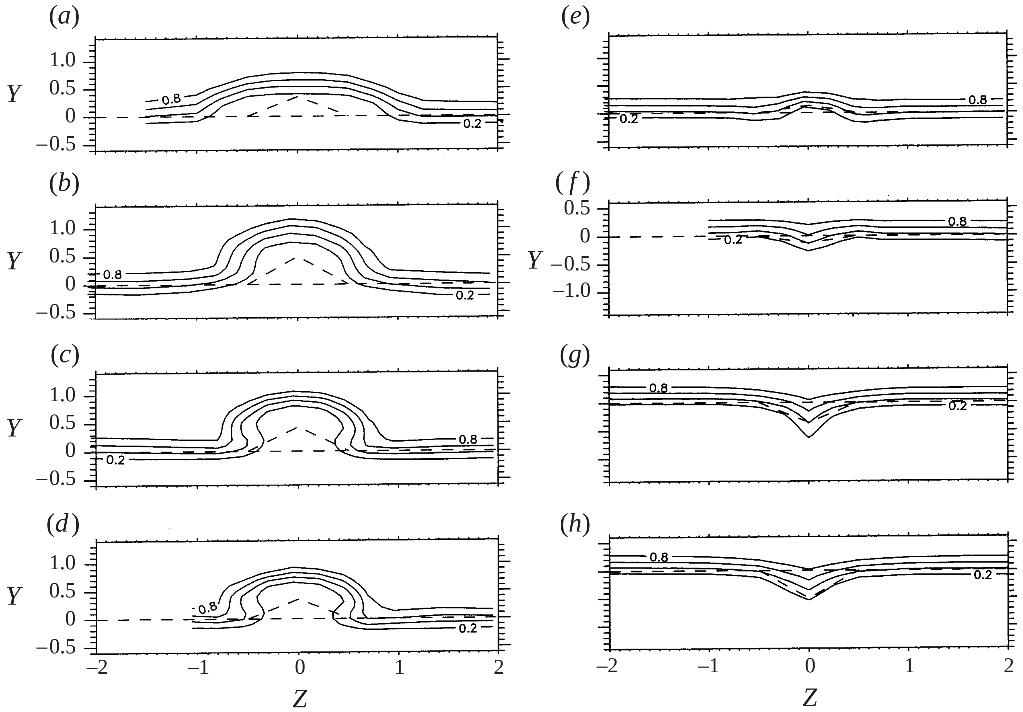

FIGURE 4. Mean velocity contours, $U(Y,Z;\theta) = 0.2, 0.4, 0.6$ and 0.8, for various angles, θ, at $X = 4.0$: (*a*) $\theta = 135°$; (*b*) 90°; (*c*) 60°; (*d*) 45°; (*e*) 15°; (*f*) −15°; (*g*) −45°; (*h*) −90°.

for brevity). In these cases, the bulk of the oncoming flow is merely deflected by the tab, because the tab surface is angled downstream. At $\theta = 135°$ and 90°, on the other hand, the oncoming flow is clearly stagnated on the tab's surface. In the latter cases (figures 4*a* and 4*b*), the contour images do not exhibit a horseshoe shape and a more significant portion of the flow is redirected in the spanwise direction. This 'spanwise jetting' is particularly noticeable in the wide and shallow contour image of $\theta = 135°$. At $\theta = 15°$ (figure 4*e*), the projected tab height is less than 30% of the boundary-layer thickness; a minimal effect is expected and observed. For all negative angles, where the tab is pitched into the low-speed side, a different picture appears. The velocity contours are almost cusped at $Z = 0$. These trends are further illuminated by an examination of the streamwise vorticity, discussed next.

The corresponding mean streamwise vorticity data are shown in figure 5. The streamwise vorticity is concentrated near the base of the tab. Solid and dotted contour lines denote positive and negative values, respectively. In each case, a pair of counter-rotating streamwise vortices with clearly identifiable cores, is evident. Recall that the streamwise vorticity generated by the pressure hill mechanism directs the flow from the tab base to the apex. The vortex pairs in all cases of figure 5, including the change in sign of Ω_x across $\theta = 0°$, indicate the dominance of this mechanism.

The motion induced by the vortex pair is obviously strongest between the cores. Thus, the cusp-shaped mean velocity profiles for $\theta < 0°$ are a result of the high-speed fluid being forced through the fairly narrow corridor between the cores. An explanation for the horseshoe/no-horseshoe shape in the positive angle cases is also apparent from the streamwise vorticity. The magnitude and compactness of the cores for $\theta = 60°$ and 45°, figure 5(*c*, *d*), is sufficient to perceptibly induce high-speed fluid

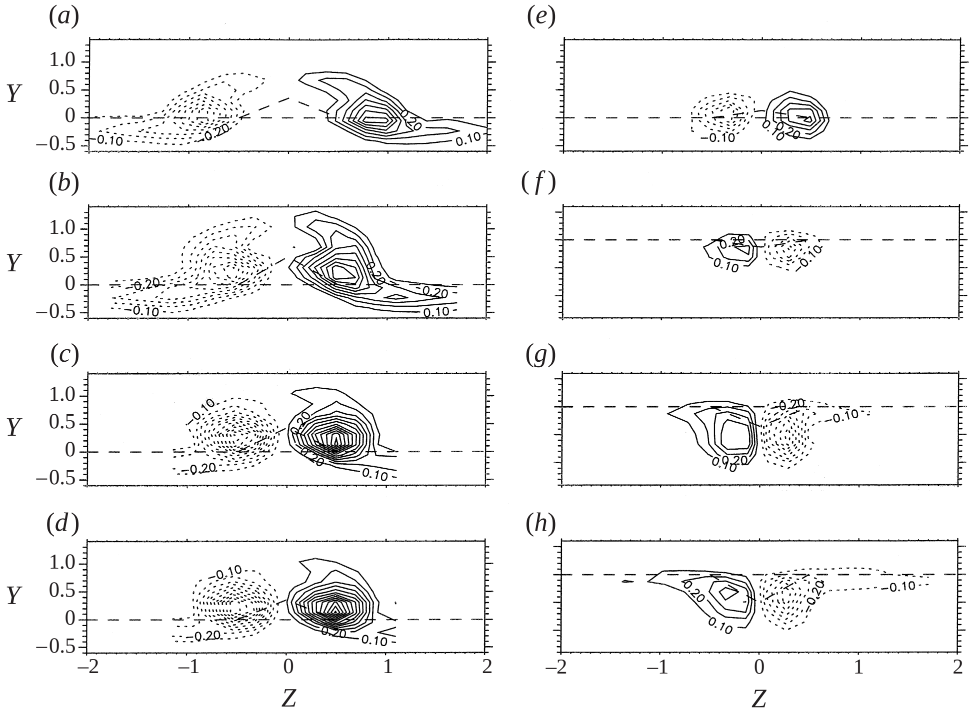

FIGURE 5. Streamwise vorticity contours $\Omega_x(Y, Z; \theta)$, for various angles, θ, as in figure 4. The minimum magnitude shown is 0.1; the increment is 0.1. The maximum contour values are: (*a*) 0.7; (*b*) 0.8; (*c*) 1.2; (*d*) 1.2; (*e*) 0.5; (*f*) 0.3; (*g*) 0.4; (*h*) 0.4. Dotted contours denote negative values.

into the shear region laterally (in z). For $\theta = 135°$ and $90°$, figures 5(*a*) and 5(*b*), however, this effect is not manifest because the cores are weaker and further apart.

Note that the deepest penetration of the high-speed fluid into the low-speed side occurs for $\theta = -45°$ (in figure 5*g*), as opposed to $-90°$ (in figure 5*h*). While the streamwise vorticity seems to be the dominant factor in this transport process, the angled surface allows for the Coanda effect (see e.g. Schlichting 1979). Consideration of the Coanda effect is what prompted Bohl & Foss (1996) to place two smaller tabs on either side of a primary tab in a square jet; the primary tab tilted into the jet stream and the secondary tabs tilted into the surroundings. This configuration increased the flux of streamwise vorticity and the mass entrainment as compared to the single, primary-tab case.

The small-scale populations corresponding to the data of figures 4 and 5 are shown in figure 6. The profile, $N^*(Y)$, is Gaussian for a two-stream shear layer; the time-averaged values peak in the centre of the shear layer (spanwise vorticity) and, of course, fall to zero in the potential regions (Huang & Ho 1990; Foss 1994; Zohar & Ho 1996). The data in figure 6 are normalized by the maximum of the two-dimensional profile (a fixed number that is determined from the measured value at $Z = 2$), $N(Y, Z; \theta) = N^*(Y, Z; \theta)/N^*_{2D\_max}$. Values greater than one, therefore, indicate the increase due to the tab. For positive angles, two regions of peak N appear on either side of the base of the tab. These maxima are in close proximity to, but not coincident with, the streamwise vortex cores. For negative angles, a dramatically different image emerges; a single peak region is centred behind the tab. The discrepancy in relative location of the peak Ω_x and N are shown in figure 7 for one positive and one negative

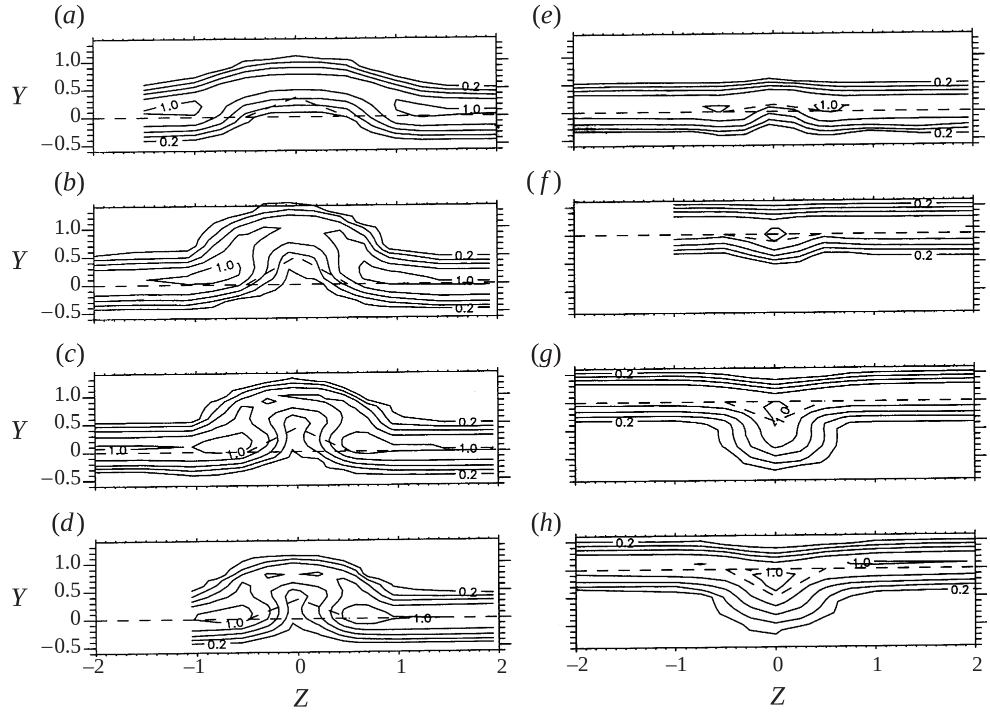

FIGURE 6. Small-scale population contours, $N(Y,Z;\theta) = 0.2$, 0.4, 0.6 and 0.8, for various angles, θ, as in figure 4.

angle. The peak small-scale populations, for all angles, consistently occur where the more energetic high-speed fluid is introduced into the shear region. (The data in figure 7 are further discussed later.) This convective transport is compatible with the coherent vortex motions shown in figure 5. This observation is similar to that of Huang & Ho (1990), but a distinction should be made. Based on observations with a coarse grid, they had stated that 'the random fine eddies are first detected in the cores of the steamwise vortices'. Careful inspection of their figure 16 shows that the peaks of small-scale population and the cores of streamwise vorticity are not exactly aligned. The data of Foss (1994), taken in the same facility with a slightly finer spanwise grid, more clearly show the lack of alignment. There is agreement on the crucial point, and it is neatly stated in Huang & Ho's conclusion: 'the random fine eddies were produced by the interactions of the merging spanwise structures and the streamwise vortices'. As discussed in § 1.2, this is borne out by several other researchers who have found that introducing streamwise vorticity into the spanwise vorticity of a shear layer also hastens the small-scale transition (see Nygaard & Glezer 1991; Moser & Rogers 1993; Zhang & Schneider 1995; Zohar & Ho 1996). It seems clear that the addition of streamwise vorticity to spanwise vorticity elevates the small-scale population. This will be quantified next.

The effect of the tab pitch angle on the large-scale vortical motions is summarized in figure 8. Here, for the left-hand side of the cross-sectional plane at $X = 4$, the peak streamwise vorticity amplitude, Ω_{x_max}, and the circulation, Γ_{LHS}, are plotted versus θ. The circulation, incidentally, was calculated via both the line integral of velocity and the area integral of vorticity; the calculations agreed within about 5%. Both plots are antisymmetric about $\theta = 0°$. In fact, had the vorticity been normalized by the local

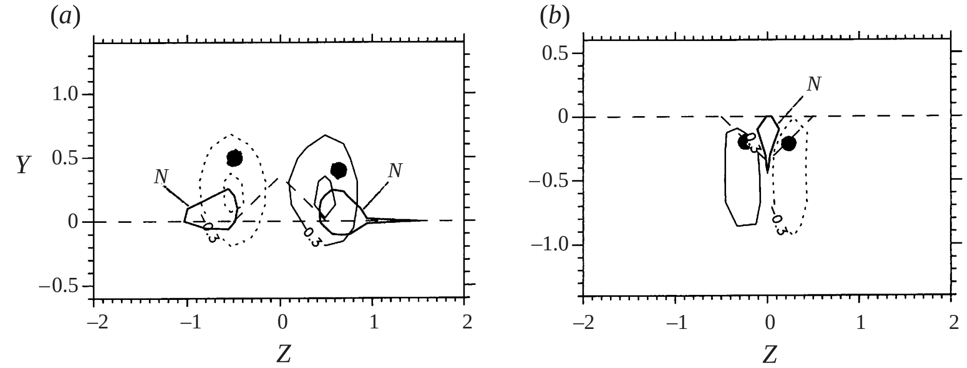

Figure 7. Comparison of relative distributions of Ω_x, $\Delta U/\Delta Z|_{max}$ and N for two angles at $X = 4.0$. Contours of Ω_x (solid and dotted lines), $\Delta U/\Delta Z|_{max}$ (dot) and N (thick solid line). (*a*) $\theta = +45°$, (*b*) −45°.

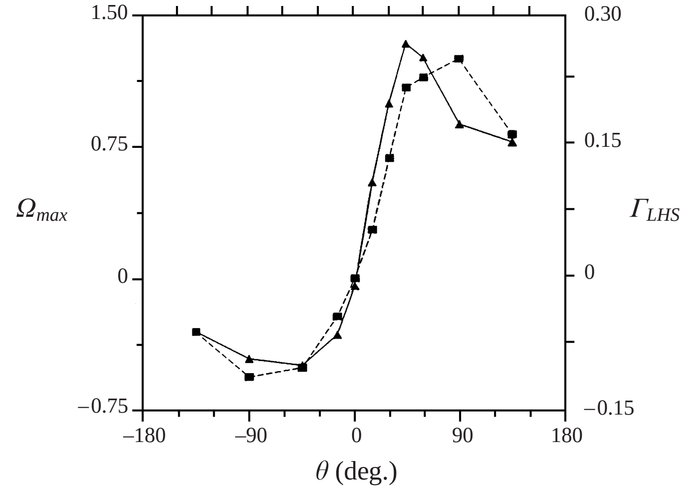

Figure 8. ▲, Peak streamwise vorticity, Ω_{x_max}, and ■, circulation (left-hand side), Γ_{LHS} *vs.* angle, θ, at $X = 4.0$.

free-stream velocity instead of the shear velocity, even the absolute magnitudes would match. The observed trends are these: both $|\Omega_{x\_max}|$ and $|\Gamma_{LHS}|$ increase with $|\theta|$ in the range $0° < |\theta| < 45°$. At $|\theta| = 45°$, $|\Omega_{x\_max}|$ reaches its peak value. For $45° < |\theta| < 90°$ $|\Omega_{x\_max}|$ decreases while $|\Gamma_{LHS}|$ continues to increase until $|\theta| = 90°$. That is, while the point measurement of core amplitude starts to decrease, the area integral of the vorticity continues to increase. For $|\theta| > 90°$, both quantities decrease.

A qualitative explanation of the trends shown in figure 8 can be reasoned as follows. As $|\theta|$ is increased from 0°, the approach flow is increasingly deflected by the tab with a corresponding increase in the amplitude of the pressure hill. The pressure build-up upstream of the tab should approximate the dynamic pressure corresponding to the velocity component normal to the tab surface. Thus, the pressure build-up reaches a maximum at $|\theta| = 90°$, when the approach flow impacts normally to the tab surface. Therefore, until 90°, the strength of the source of streamwise vorticity from the pressure hill (source 1) increases with $|\theta|$. For $|\theta| > 90°$, the approach flow is still stagnated by the tab (at $Z = 0$), and hence, the amplitude of the pressure hill remains unchanged. The notion of such pressure variation with θ is supported by the static pressure data presented by Zaman *et al.* (1994). The data show a large increase in the peak pressure amplitude as θ is increased from 45° to 90° but only a slight increase as θ is increased from 90° to 135° (note that the reference for θ, and the geometry of the tab at 90°, are different in the cited work). Thus, with increasing $|\theta|$ until 90°, an increase in the amplitude of the pressure hill causes an increase in $|\Gamma_{LHS}|$. For $|\theta| > 90°$, however, streamwise vorticity from source 2 (i.e. vorticity shed from the edges of the tab and reoriented downstream; see the reference cited above and the discussion in § 1.1) is of opposite sign counteracting the vorticity from the pressure hill. Introduction of vorticity of opposite sign is thought to be the main reason for the decrease in the circulation at the larger angles. Thus, the peak in $|\Gamma_{LHS}|$ occurs at $|\theta| = 90°$.

Vorticity from source 2 is also thought to be responsible for the occurrence of the $|\Omega_{x\_max}|$ peak at $|\theta|$ less than 90°. At smaller angles, when the tab leans downstream, the vorticity shed from the edges of the tab is reoriented into streamwise component with relative ease by the velocity gradient. The reoriented vorticity reinforces the vorticity from the pressure hill resulting in higher peak magnitudes. As $|\theta|$ approaches 90°, much of the vorticity from source 2 not only takes a longer distance to reorient itself but also is farther apart from the cores of the pressure hill vorticity. Thus, even though the net circulation is larger at $|\theta| = 90°$, the distribution of Ω_x over a larger area results in a smaller $|\Omega_{x\_max}|$.

Of considerable interest and much speculation is the issue concerning the origin of the small-scale structures. We have already observed with figures 6 and 7 that the addition of streamwise vorticity elevates small-scale population. In this experiment, by changing θ, the magnitude of the streamwise vorticity is changed incrementally for a given approach spanwise vorticity. The resulting effect on the small-scale population is further analysed. An overall measure of the small-scale population was formulated for this purpose. The $N(Y, Z)$ data were integrated over the data plane for each angle. Specifically, the $N(Y)$ profiles were integrated first. To isolate the effect of the tab, the amount $\int N(Y)\mathrm{d}Y$ from the two-dimensional region was subtracted. Then these values were integrated over the span. This final integrated value, N_{int}, is expressed as,

$$N_{int} = \int \left\{ \int N(Y, Z)\mathrm{d}Y - \int N_{2-D}(Y)\mathrm{d}Y \right\} \mathrm{d}Z.$$

The result is shown in figure 9. The two peaks for N_{int} occur at $\theta \approx \pm 60°$ close to the $|\Omega_{x\_max}|$ peak. The overall trend, as will be further supported by data presented in the next sections, quite clearly show that an incremental change in θ changes both $|\Omega_x|$ and N_{int} in the same way. The number of small-scale structures generated is strongly correlated to the magnitude of the streamwise vorticity.

While a full explanation for the correlation observed in the foregoing is beyond the scope of the present experimental study, the following may be noted. Huang & Ho (1990) had proposed that the increased strain rate due to the interaction of the large-scale vortical motions ($\Omega_z - \Omega_z$, $\Omega_z - \Omega_x$) is responsible for generating the small-scale eddies. The present results are consistent with this postulate. Another possible mechanism for the increased number of small-scale eddies is the flow instability due to the additional inflection points created by the tabs. Nygaard & Glezer (1991) identified the inflection points in their $U(Z)$ profile, caused by the 'streamwise' vorticity (which had a definite Ω_y component), as locally unstable regions of large shear. These regions underwent rapid amplification, then broke down into small-scale motions. As can be discerned from figure 4, the $U(Z)$ profiles in the present experiment also have

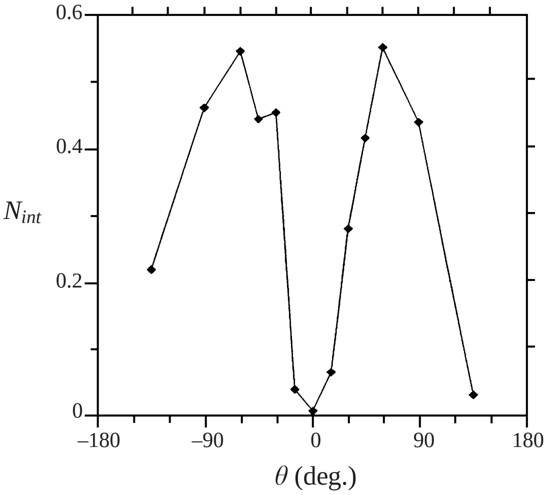

FIGURE 9. Integrated small-scale population, N_{int}, *vs.* angle, θ, at $X = 4.0$.

inflection points around the tab. The two locations of peak $|\Delta U/\Delta Z|$ are depicted with large dots in figure 7. The peak locations can be seen to occur close to the locations of $|\Omega_{x\_max}|$. Furthermore, the maximum amplitude of $|\Delta U/\Delta Z|$ occurred for $\theta = 45°$ and 60° (the normalized central difference values were 2.15 and 2.11, respectively.) Thus, the instability due to the additional inflection points (in the $U(Z)$ profile) as the cause for increased small-scale population is also supported by the present results.

Additional insight into mixing transition and generation of small-scale structures comes from several other investigations. Hu *et al.* (1996) observed that the streamwise vorticity, Ω_x, accelerates the instability of the primary vorticity, Ω_z; then, viscous diffusion accelerates the transfer of energy and vorticity to smaller scales. A spectral approach analysing the energy transfer to smaller scales (higher wavenumbers) is based on triadic interaction among scales (Domaradzki 1990; Yeung 1996). Coupling between large and small-scale structures in physical space has also been analysed through direct numerical simulation by Melander & Hussain (1993). Also notable in this connection is the notion of the existence of a mixing transition Reynolds number (Dimotakis 1993), mixing transition based on the number of vortex pairings (Karasso & Mungal 1996), and the concept of 'core dynamics instability' of spanwise vortices (Schoppa Hussain & Metcalfe 1995).

We conclude this section by noting, once again, that the optimum angle for obtaining the largest small-scale population and strongest streamwise vorticity is in the θ range of 45°–60°. From flow blockage (and hence, momentum or thrust loss) considerations the smaller angle $\theta = 45°$ is used for the rest of the study.

3.2. *Single tab; flow field evolution*

The downstream evolution of the flow behind a single tab at $\theta = 45°$ was explored. Data were sampled at four locations, $X = 1.0$, 2.0, 4.0 and 8.5. For this set of experiments, the data were taken over a smaller window. The mean velocity contours, $U(Y, Z; X)$ are shown in figures 10(*a*)–10(*d*). Corresponding distributions of $\Omega_x(Y, Z; X)$ and $N(Y, Z; X)$ are shown in figures 10(*e*)–10(*h*) and figures 10(*i*)–10(*l*), respectively. Behind the tab apex at $X = 1.0$, figure 10(*a*), the shear is high. A close inspection should reveal the still present wake (dotted contour) near the tab apex. The

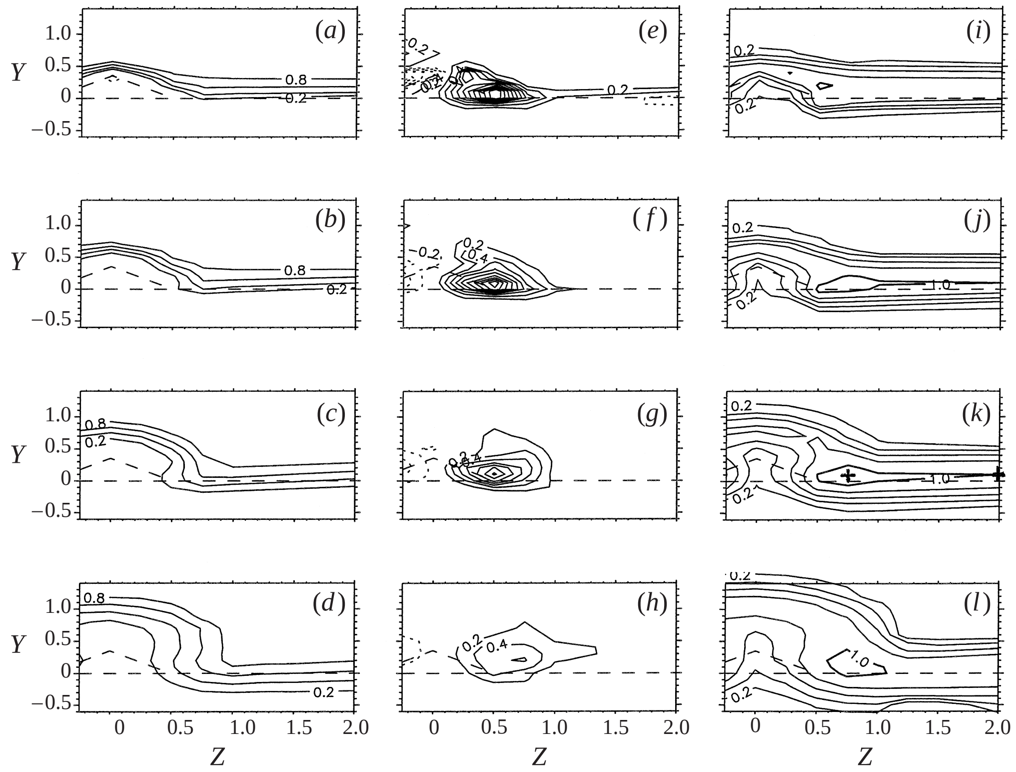

FIGURE 10. Downstream evolution of U (in (*a*)–(*d*)), Ω_x (in (*e*)–(*h*)) and N (in (*i*)–(*l*)) for a single tab at $\theta = 45°$. $X = 1.0$ (*a, e, i*); 2.0 (*b, f, j*); 4.0 (*c, g, k*); 8.5 (*d, h, l*).

contour lines are essentially parallel to the tab and splitter plate trailing edges. The streamwise vorticity is most intense at this most upstream location, figure 10(*e*). There is even a hint of the necklace vorticity (far right in figure 10(*e*) which has a sense counter to the pressure hill vorticity (Bohl & Foss 1996). At $X = 2.0$, figure 10(*b*), the mean velocity distortion caused by the tab has grown more in Y than in Z. This is expected because of the motion induced by the streamwise vorticity, figure 10(*f*). The horseshoe pattern in the mean velocity distribution appears by $X = 4.0$ (figure 10*c*), and persists through $X = 8.5$ (figure 10*d*).

It is clear that the streamwise vorticity persisted at the farthest X (figure 10*h*). At all X, the relative strength of the streamwise vorticity remained nominally constant at 80% of the spanwise vorticity, as estimated from $\Delta U/\Delta Y$. In other words, $\Omega_{x\_max}/\Omega_{z\_max} = O(1)$. This is in contrast to the effect of the tab with a circular jet issuing into quiescent surroundings for which the relative strength ratio was only 20% (Zaman 1993). This difference is believed to be primarily due to the presence of the co-flow. The streamwise vorticity generated by the tab placed in the higher-speed stream should remain the same; addition of the co-flow reduces the amplitude of the spanwise vorticity. Thus, the ratio of the amplitude $\Omega_{x\_max}/\Omega_{z\_max}$ is increased.

The small-scale populations in figures 10(*i*)–10(*l*), as before, are normalized by the peak two-dimensional population. The peak two-dimensional value at each X location is used for normalizing the respective data, $N(Y, Z; X) = N^*(Y, Z; X)/N^*_{2D\_max}(X)$. Thus, the normalization accounts for the growth of the small-scale population with increasing X. The data in figures 10(*i*)–10(*l*) illustrate that the increased population

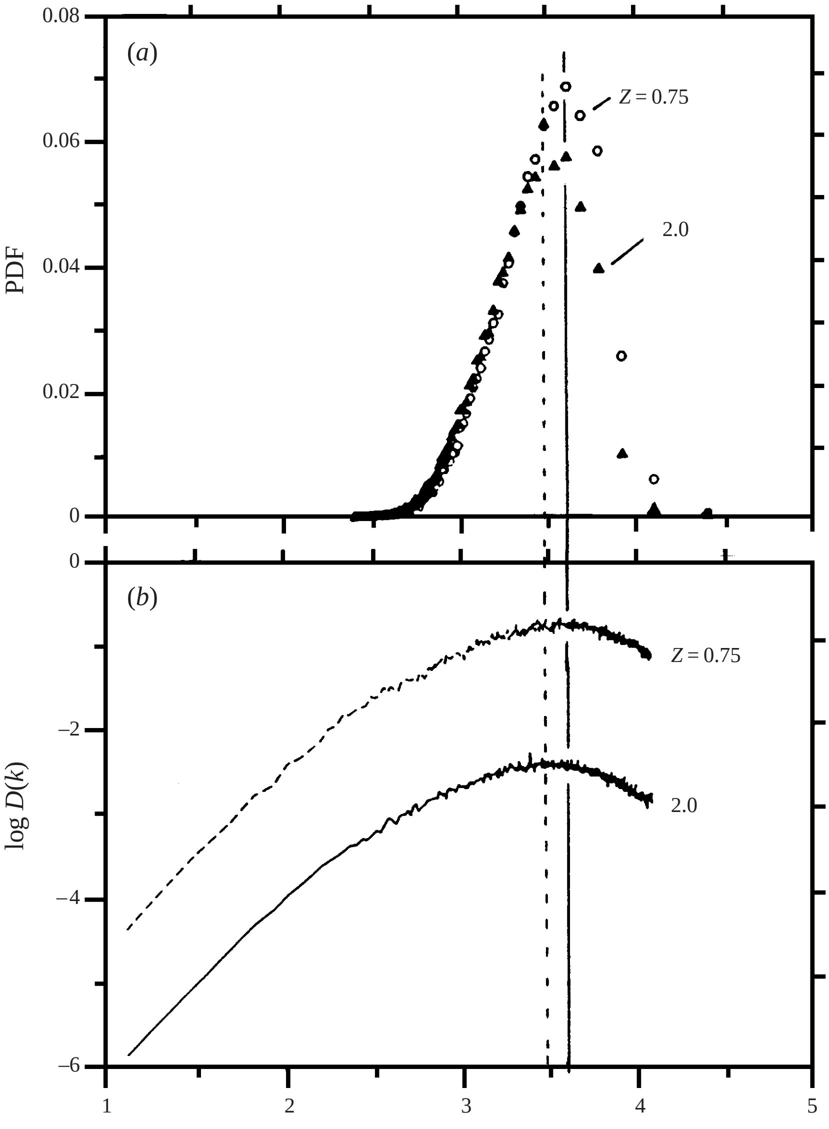

FIGURE 11. Comparison of small-scale characteristics at cross-hair locations identified in figure 10(*k*): (*a*) PDF of frequencies, (*b*) pseudodissipation spectra.

occurs near the cores of the streamwise vortex for all X. It should be apparent that the inferences made from the data of figure 7 should be valid for all X.

The tab also altered the frequency characteristics of the fine-scale eddies. In order to illustrate this, data from two points on the $X = 4.0$ plane are compared. The locations are marked with cross-hairs in figure 10(*k*); one is at the location of peak small-scale population, $Z = 0.75$, the other is at the location of maximum population in the two-dimensional region at $Z = 2.0$. The histograms of the small-scale frequency and dissipation spectrum, determined from pulse trains similar to that in figure 2, are shown in figure 11. The most probable frequency in the two-dimensional ($Z = 2.0$) region is 3.1 kHz (log(frequency) = 3.49). At the base edge of the tab, it increases to

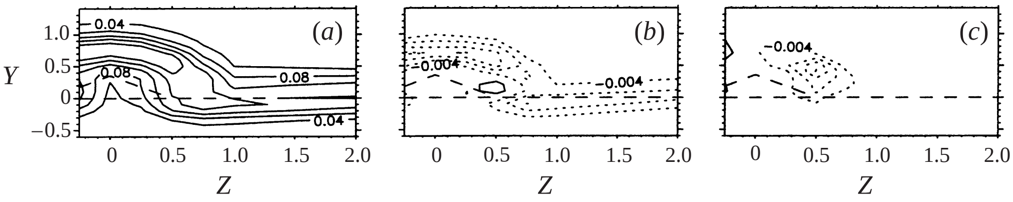

FIGURE 12. Turbulence characteristics at $X = 4.0$ and $\theta = 45°$, (*a*) u', (*b*) $\overline{u'v'}$ and $\overline{u'w'}$. Contour increment is 0.04 in (*a*) and 0.004 in (*b*) and (*c*).

4.2 kHz (log(frequency) = 3.62). These values are confirmed by the one-dimensional pseudodissipation spectra (see the discussion in § 2.1). Thus, the tab not only generated more small scales but it also made them smaller.

Additional turbulence quantities are shown in figure 12. The pattern of contours for the streamwise r.m.s. velocity, u', presented in figure 12 (*a*), is representative of both secondary r.m.s. velocities, v' and w', and of all X locations. In all of these maps, the region of peak r.m.s. velocity occurs not near the location of maximum small-scale population, but where the shear is highest. Recall that the PVC technique filters out all but the dissipative eddies, whereas the r.m.s. calculation includes all scales. Referring to the mean velocity profiles in figure 3, the r.m.s. velocity can be seen to peak at the main shear-layer inflection-point. The small-scale population, on the other hand, peaks near the bump in the mean velocity profile produced by the tab.

The time-averaged Reynolds stresses, $\overline{u'v'}$ and $\overline{u'w'}$ are shown in figures 12 (*b*) and 12 (*c*), respectively. As expected for a mixing layer, the $\overline{u'v'}$ is negative in the shear regions, and the $\overline{u'w'}$ is aligned with and opposite in sign to the streamwise vorticity (Bell & Metha 1993; Foss 1994). The fact that the two stress terms have nominally the same magnitude further delineates the effect of the tab on the flow field. Recall that the component vorticities had nearly the same magnitude, $\Omega_{x\_max}/\Omega_{z\_max} = O(1)$. The positive region of $\overline{u'v'}$ (figure 12 *b*) occurs with the counter-gradient of $U(Y)$, seen in figure 3. This positive region is first evident at $X = 2.0$ and persists beyond $X = 8.5$, as does the mean velocity bump. While the streamwise vorticity is most intense at $X = 1.0$, its effect on the flow field has not yet been realized in terms of substantial momentum transfer. Once the effect is realized, the pattern of the flow field remains similar thereafter within the measurement range covered. Both production terms, $P = -\overline{u_i u_j}(\partial U_i/\partial x_j)$, remain positive everywhere; the energy transfer is always from the mean to the turbulent motions.

3.3. *Multiple tabs*

The final issue addressed in this paper is the effect of spacing, S, for a multiple tab array. Four tabs at $\theta = 45°$ were investigated for this part of the study. Figure 13 shows a window of the $U(Y, Z; S)$ contour plots at two cross-stream planes, $X = 4.0$ and 7.5. A larger 'two-dimensional' region was needed for the multiple tab experiment, this restricted the choice of the farthest downstream location to $X \leqslant 7.5$. Data are shown in figure 13 for four spacings, $S = 3.0$, 1.5, 1.25 and 1.0. The central two tabs are always shown; they also depict the spacing.

For $S = 3.0$, the tabs behave as if they are isolated within the measurement domain. This can be seen by comparing the mean velocity contours with those for the isolated tab: figure 13 (*a*) with figures 4 (*d*) and 10 (*c*) for $X = 4.0$, and figure 13 (*e*) with figure 10 (*d*) for $X \approx 8$. The deflection behind the tab appears the same, as

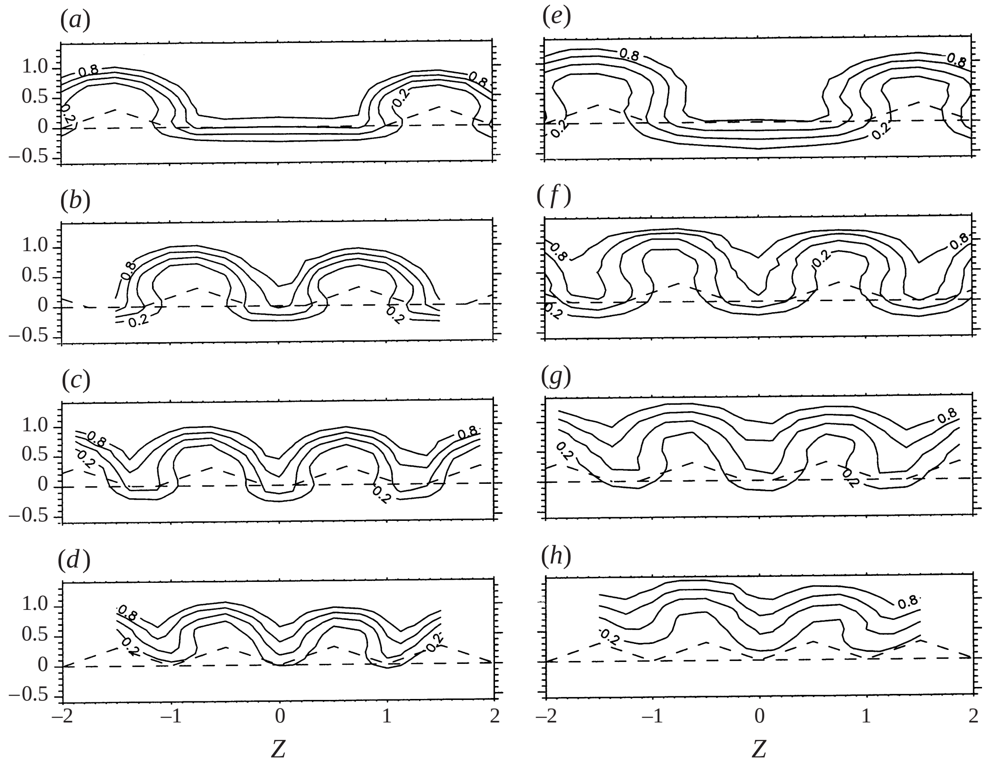

Figure 13. Mean velocity contours, $U(Y,Z;S) = 0.2$, 0.4, 0.6 and 0.8, at various separations, S. For $X = 4.0$: (*a*) $S = 3.0$, (*b*) 1.5, (*c*) 1.25, (*d*) 1.0. For $X = 7.5$: (*e*) $S = 3.0$, (*f*) 1.5, (*g*) 1.25, (*h*)1.0.

does the nominally two-dimensional region away from the tab. However, there are perceptible differences. The largest difference is in the 'drop' of the two-dimensional region between tabs. This lowering of the shear layer is a result of the induced motion of the pair of streamwise vortices that span the two-dimensional region in the multiple tab case (figures 13 *a* and 13 *e*). In the single tab case on the other hand, there is only one streamwise vortex on one edge of the two-dimensional region (figures 10 *c* and 10 *d*).

Data taken at $S = 2.0$, not shown for brevity, are similar to those at $S = 3.0$; a distinct two-dimensional region exists. This is no longer the case for $S = 1.5$ as shown in figures 13 (*b*) and 13 (*f*). Although the location of the distorted contours and the two-dimensional region have not changed substantially at $X = 4.0$, the shear layer has been displaced upward at $X = 7.5$. For the closest spacing, $S = 1.0$, the centre of the shear layer was displaced substantially toward the high-speed side (figures 13 *d* and 13 *h*). This rise is apparently caused by the 'vectoring' effect of the tabs. The solidity of the array at the smallest spacing is sufficient to make it act like a solid deflector. It can be observed from the data of figure 13 that this flow vectoring increases as S decreases and as X increases.

The streamwise vorticity contours, $\Omega_x(Y, Z; S)$, are shown in figure 14. The contour window has been widened to include the flow field outside of the tab array. In each of figures 14 (*a*) and 14 (*b*), approximately three vortex pairs are captured within the measurement domain. The uniformity in the distribution and magnitudes of the vortices for $S = 3.0$, shown in figures 14 (*a*) and 14 (*e*), confirms the weakness of the

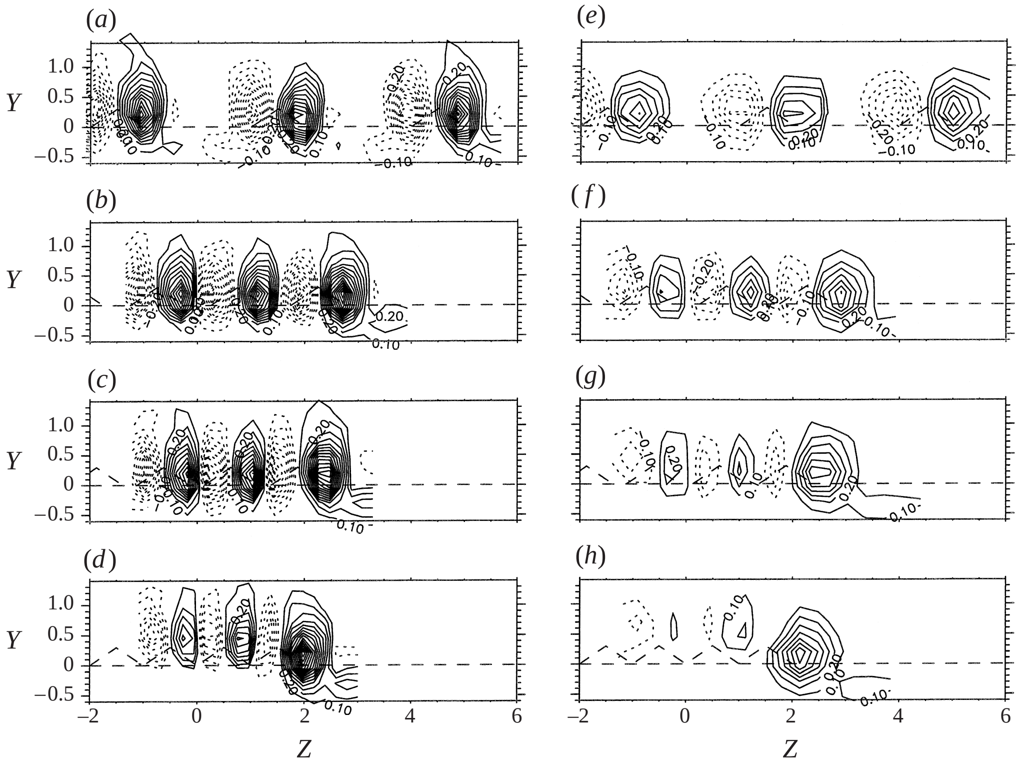

FIGURE 14. Streamwise vorticity contours, $\Omega_x(Y,Z;S)$, at various separations, S, as in figure 13. The minimum magnitude shown is 0.1; the increment is 0.1. Dotted contours denote negative values.

flow interaction between tabs at this spacing. In figure 14(*b*), for $S = 1.5$, $X = 4.0$, the core magnitudes remained nominally the same as for $S = 3.0$, however, there is a slight spanwise variation, i.e., the outermost positive vortex core is stronger than the inner positive cores. This trend is accentuated with increasing distance and decreasing spacing. In the limit, $S = 1.0$, $X = 7.5$, (figure 14*h*), the outside vortex is nominally seven times more intense than the inner vortices. Continuing with the 'solid deflector' analogy, the array of tabs may be thought of as acting like a single tab. The outer vortex is then a component of the counter-rotating vortex pair from that 'single' tab. The corresponding small-scale populations, $N(Y, Z; S)$ are shown in figure 15. Data are shown only for $X = 4$ which are deemed sufficient to illustrate the essential trends. Again, data for the largest spacing are similar to that for the isolated tab case, compare figure 15(*a*) with figure 10(*k*). At the intermediate spacings, the peak population increases somewhat near the base of the tab. These differences are not easily discernible from the contour plots, and are further analysed in the following.

The momentum thickness, δ_θ, was calculated from the mean velocity profiles at each Z location (figure 13). Averages, $\overline{\delta_\theta}$, taken over $Z \in \left[-\frac{1}{2}S, \frac{1}{2}S\right]$ are listed in table 1. As can be seen, any tab configuration nearly doubled $\overline{\delta_\theta}$ compared to the unperturbed case. According to this thickness measure, the 'best' case is $S \approx 1.5$. Of course, the thickening of the shear layer is an indication of increased entrainment. The peak amplitudes of the streamwise vortex pairs from the inner two tabs (figure 14) were averaged, and also listed in table 1 as $\overline{\Omega}_{x\_max}$. This measure indicates that the wider spacings are advantageous so that vorticity from one tab does not interfere or

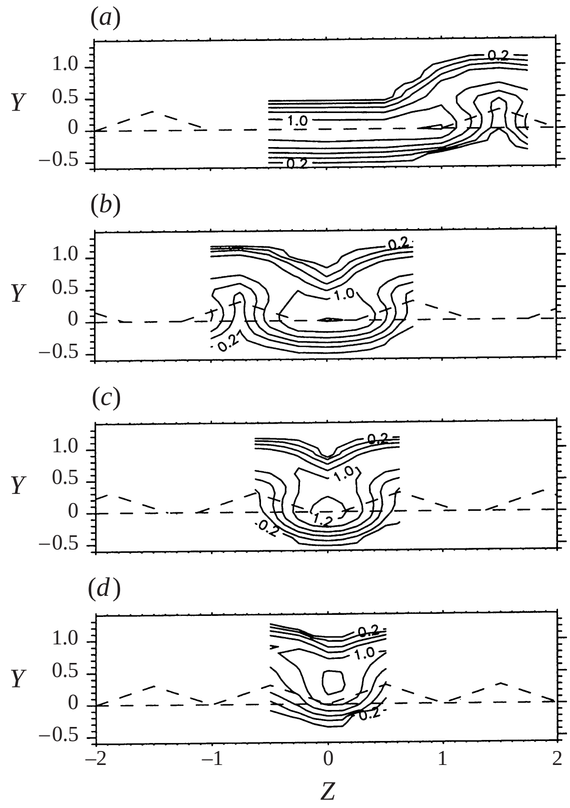

Figure 15. Small-scale population distributions, $N(Y, Z; S)$, at various S, as in figure 13, for $X = 4.0$ only.

S	$\overline{\delta_\theta}$	$\overline{\Omega}_{x\_max}$	N_{int}
No tabs	0.08	–(0)–	0.02
3.00	0.14	1.23	—
2.00	0.18	—	0.24
1.50	0.18	1.23	0.25
1.25	0.18	1.10	0.22
1.00	0.16	0.62	0.19

Table 1. Comparison of average momentum thickness, $\overline{\delta_\theta}$, peak streamwise vorticity magnitude, $\overline{\Omega}_{x\_max}$ and integrated small-scale population, N_{int}, for various spacings, S, at $X = 4.0$.

annihilate that from its neighbour. Table 1 also lists N_{int} averaged over $Z \in \left[0, \frac{1}{2}S\right]$. By definition, the value of N_{int} for the no-tab case should be identically zero (0); the non-zero value is an indication of the error, which comes primarily from the tails of the integrand. The value of N_{int} is not shown for $S = 3$ because of erroneous contribution from the long two-dimensional region; for $S = 2$ only single-wire data were obtained, thus, $\overline{\Omega}_{x\_max}$ is not available; and for the no-tab case, Ω_x was not measured and presumed to be zero. The 'mixing metrics' outlined in table 1 do not readily suggest an obvious optimal spacing. However, considering all parameters, the most effective spacing is inferred to be in the range, $S \approx 1.5$.

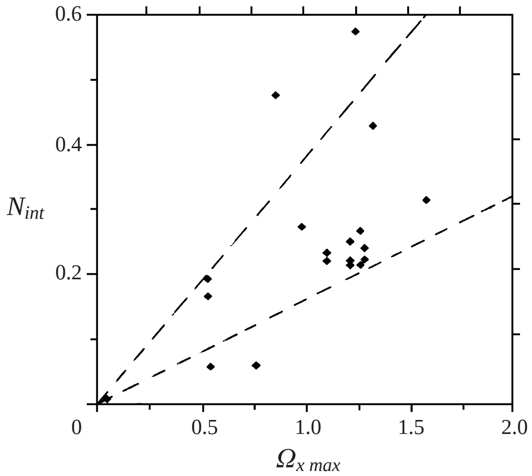

FIGURE 16. Integrated small-scale population, N_{int}, *vs.* peak streamwise vorticity, Ω_{x_max}, for all $\theta > 0$ cases.

We have seen before that the overall small-scale population is strongly correlated with the amplitude of streamwise vorticity. This trend is also reflected in the measurements for the multiple tab array. Recall that the outer-most vortex in the multiple-tab array was stronger than the inner vortices. For example, for $S = 1$ at $X = 4$ (figure 14) the peak Ω_x in the outer vortex was nominally three times the corresponding peak values in the inner ones. The magnitude of N_{int} was also found to be nominally three times larger in the outer vortex region than in the inner vortices. This trend is substantiated in figure 16, where N_{int} versus Ω_{x_max} is plotted for all cases studied including the outer vortices in the multiple-tab array. Most of the data fall within a wedge, clearly showing that the more intense the streamwise vorticity the greater the overall small-scale population.

4. Concluding remarks

The influence of an array of delta tabs on the large- and small-scale mixing characteristics in a 2:1 velocity ratio shear layer was studied experimentally. The objective was to determine the optimal tab configuration for the maximum mixing as determined by both time-averaged vorticity magnitudes and small-scale populations. Two parameters, the pitch angle, θ, for a single tab and the spanwise spacing, S, for an array, were varied.

The magnitude of the circulation generated by a single tab, on either side of its symmetry plane, was found to vary directly with variation of the pitch angle $|\theta|$. The maximum in the circulation occurred when the tab was placed normal to the flow ($|\theta| = 90°$). The streamwise vorticity, however, was more concentrated, and hence, its peak magnitude ($|\Omega_{x\_max}|$) was the largest when the apex of the tab was tilted downstream at $|\theta| \approx 45°$. The integrated small-scale population (N_{int}) was also found to vary with $|\theta|$. The maximum in N_{int} occurred at $|\theta| \approx 60°$, at approximately the condition where $|\Omega_{x\_max}|$ peaked. For an array of tabs, the spacing between tabs (S) affected the downstream flow. Within the measurement domain ($X \approx 8$), the tabs acted as if isolated for $S = 3$. With contiguous tabs ($S = 1$), on the other hand, the array acted as a solid deflector. In the latter case, the streamwise vorticity magnitude, as well as the small-scale population, were the smallest directly downstream of the array. The streamwise vorticity distribution, however, rearranged such that the two vortices on either end were strengthened. It was as if the array acted as a single, wide tab. The small-scale population in the outer vortex region was found to be proportionately larger. The optimum spacing, based on the largest average thickness of the mixing layer, the strongest streamwise vorticity magnitude, as well as the largest small-scale population, was inferred to be $S \approx 1.5$.

Perhaps the most significant result obtained in this investigation is the relationship between peak streamwise vorticity (Ω_{x_max}) and the small-scale population (N_{int}). For all cases surveyed, there was a direct correlation; the larger the Ω_{x_max}, the larger the N_{int}. The location of peak small-scale population, N, occurred in the centre of the shear layer, and on the 'high-speed' side of the Ω_x core, i.e. where the high-speed fluid entered the shear region. The location of peak r.m.s. velocities, on the other hand, did not coincide with that of peak N. The r.m.s. peaks occurred in regions where the shear was maximum. At locations where the small-scale population was concentrated, the turbulent structures also shifted to higher frequencies. The tab not only generated more small-scale structures, but it made them smaller as well.

The authors are indebted to Professor John F. Foss of Michigan State University for valuable inputs in this research as well as for a review of the manuscript. The first author is thankful to the NRC/NASA post-doctoral fellowship program for support during the course of this work.

REFERENCES

Ahuja, K. K. 1993 Mixing enhancement and jet noise reduction through tabs plus ejectors. *AIAA paper* 93-4347, 15th Aeroacoustics Conference, Long Beach, CA, 25–27 October.

Ahuja, K. K. & Brown, W. H. 1989 Shear flow control by mechanical tabs. *AIAA Paper* 89-0994.

Bell, J. H. & Metha, R. D. 1990 Interaction of a streamwise vortex with a turbulent mixing layer. *Phys. Fluids* A **2**, 2011–2023.

Bell, J. H. & Metha, R. D. 1993 Effects of imposed spanwise perturbations on plane mixing-layer structure. *J. Fluid Mech.* **257**, 33–63.

Bohl, D. & Foss, J. F. 1996 Enhancement of passive mixing tabs by the addition of secondary tabs. *AIAA Paper* 96–054.

Bradbury, L. J. S. & Khadem, A. H. 1975 The distortion of a jet by tabs. *J. Fluid Mech.* **70**, 801–813.

Carletti, M. J., Rogers, C. B. & Parekh, D. E. 1995 Use of streamwise vorticity to increase mass entrainment in a cylindrical ejector. *AIAA J.* **33**, 1641–1645.

Cetegen, B. M. & Aguirre, J. P. 1990 Analysis of molecular mixing and chemical reaction in a vortex pair. *Phys. Fluids* A **2**, 2211–2216.

Dimotakis, P. E. 1993 Some issues on turbulent mixing and turbulence. *Graduate Aeronautical Laboratories, CalTech Rep.* FM93-1.

Domaradzki, J. A. 1990 Local energy transfer and nonlocal interactions in homogeneous, isotropic turbulence. *Phys. Fluids* A **2**, 413–426.

Foss, J. K. 1994 Small-scale turbulence in a plane mixing layer. PhD thesis, University of Southern California.

Foss, J. K. & Zaman, K. B. M. Q. 1996 Effect of a delta tab on fine-scale mixing in a turbulent two-stream shear layer. *AIAA Paper* 96–0546.

Gretta, W. J. & Smith, C. R. 1993 The flow structure and statistics of a passive mixing tab. *Trans. ASME* I: *J. Fluids Engng* **115**, 255–263.

Grosch, C. E., Seiner, J. M., Hussaini, M. Y. & Jackson, T. L. 1997 Numerical simulation of mixing enhancement in a hot supersonic jet. *Phys. Fluids* **9**, 1125–1143.

Hu, H., Wu, S.-S., Shen, G.-X. & Yagoda, E. 1996 Effect of tabs on the vortical and turbulent structures of jet flows. *ASME FED* Vol. 237, pp. 77–84.

HUANG, L.-S. & HO, C.-M. 1990 Small-scale transition in a plane mixing layer. *J. Fluid Mech.* **210**, 475–500.

ISLAND, T. C., URBAN, W. D. & MUNGAL, M. G. 1998 Mixing enhancement in compressible shear layers via sub-boundary layer disturbances. *Phys. Fluids* **10**, 1008–1020.

KARASSO, P. S. & MUNGAL, M. G. 1996 Scalar mixing and reaction in plane liquid shear layers. *J. Fluid Mech.* **323**, 23–63.

MEIBURG, E. & LASHERAS, J. C. 1988 Experimental and numerical investigation of the three-dimensional transition in a plane wake. *J. Fluid Mech.* **190**, 1–37.

MELANDER, M. V. & HUSSAIN, F. 1993 Coupling between a coherent structure and fine-scale turbulence. *Phys. Rev.* E **48**, 2669–2689.

MOSER, R. D. & ROGERS, M. M. 1993 The three-dimensional evolution of a plane mixing layer: pairing and the transition to turbulence. *J. Fluid Mech.* **247**, 275–320.

NYGAARD, K. J. & GLEZER, A. 1991 Evolution of streamwise vortices and generation of small-scale motion in a plane mixing layer. *J. Fluid Mech.* **231**, 257–301.

POTTER, M. C. & FOSS, J. F. 1982 *Fluid Mechanics*, Great Lakes Press.

REEDER, M. F. & SAMIMY, M. 1996 The evolution of a jet with vortex-generating tabs: real-time visualization and quantitative measurements. *J. Fluid Mech.* **311**, 73–118.

REEDER, M. F. & ZAMAN, K. B. M. Q. 1996 The impact of tab location relative to the nozzle exit on jet distortion. *AIAA J.* **34**, 197–199.

SCHLICHTING, H. 1979 *Boundary Layer Theory*, 7th edn. McGraw-Hill.

SCHOPPA, W., HUSSAIN, F. & METCALFE, R. W. 1995 A new mechanism of small-scale transition in a plane mixing layer: core dynamics of spanwise vortices. *J. Fluid Mech.* **298**, 23–80.

STEFFEN, C. J., REDDY, D. R. & ZAMAN, K. B. M. Q. 1997 Numerical modeling of jet entrainment for nozzles fitted with delta tabs. *AIAA Paper* 97–0709.

TANNA, H. K. 1977 An experimental study of jet noise, Part II: shock associated noise. *J. Sound Vib.* **50**, 429–444.

YEUNG, P. K. 1996 Multi-scalar triadic interactions in differential diffusion with and without mean scalar gradients. *J. Fluid Mech.* **321**, 235–278.

ZAMAN, K. B. M. Q. 1993 Streamwise vorticity generation and mixing enhancement in free jets by 'delta tabs'. *AIAA Paper* 93-3253.

ZAMAN, K. B. M. Q. 1996 Spreading characteristics and thrust of jets from asymmetric nozzles. *AIAA Paper* 96-0200.

ZAMAN, K. B. M. Q., REEDER, M. F. & SAMIMY, M. 1994 Control of an axisymmetric jet using vortex generators. *Phys. Fluids* **6**, 778–793.

ZHANG, S. & SCHNEIDER, S. P. 1995 Quantitative molecular-mixing measurements in a round jet with tabs. *Phys. Fluids* **7**, 1063–1070.

ZOHAR, Y. & HO, C.-M. 1996 Dissipation scale and control of fine-scale turbulence in a plane mixing layer. *J. Fluid Mech.* **320**, 139–161.